



# Lead-free mesoscopic $\text{Cs}_2\text{SnI}_6$ perovskite solar cells using different nanostructured ZnO nanorods as electron transport layers

Xiaofeng Qiu, Yanan Jiang, Hailiang Zhang, Zhiwen Qiu, Shuai Yuan, Ping Wang, and Bingqiang Cao\*

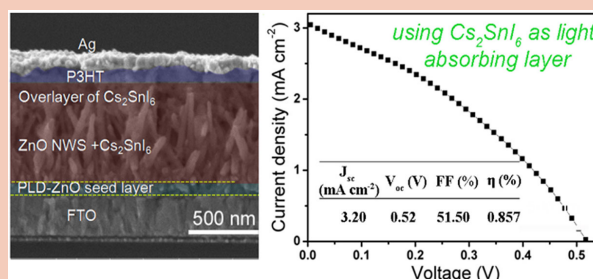
Materials Research Center for Photoelectric and Photoelectrochemical Energy Conversion, School of Materials Science and Engineering, University of Jinan, Jinan 250022, P.R. China

Received 9 June 2016, revised 27 June 2016, accepted 28 June 2016  
Published online 30 June 2016

**Keywords** perovskite, absorbers, air-stable, lead-free,  $\text{Cs}_2\text{SnI}_6$ , mesoscopic solar cells

\* Corresponding author: e-mail mse\_caobq@ujn.edu.cn

Lead-free and more air-stable perovskite  $\text{Cs}_2\text{SnI}_6$  absorber with a direct bandgap of 1.48 eV is synthesized via a modified solution process. Different nanostructured ZnO nanorod arrays as electron transport layers and hole blocking layers are grown by controlling the seed layer and used to fabricate mesoscopic perovskite solar cells with  $\text{Cs}_2\text{SnI}_6$  as light absorber layer. The influences of ZnO seed layers and nanorod morphology on the device photovoltaic performance were also investigated. With careful control of ZnO nanorod length and pore size to ensure high loading of the  $\text{Cs}_2\text{SnI}_6$  absorber, we achieved power conversion efficiency of near 1%.



© 2016 WILEY-VCH Verlag GmbH & Co. KGaA, Weinheim

**1 Introduction** Lead halide perovskite (e.g.,  $\text{CH}_3\text{NH}_3\text{PbX}_3$ , X = I, Br, Cl) solar cells have experienced the fastest increase in reported efficiencies ever obtained for any photovoltaic technology. Since a series reports of all-solid-state lead halide perovskite-based solar cells (PSCs) with efficiencies of 10% to 12% [1–3], recent progress has pushed the power conversion efficiency (PCE) up to 20% [4]. Intense researches are currently focusing on the stability of the perovskite light harvester and large-scale photovoltaic (PV) products for promising commercial propose. However, consideration over the toxicity of lead (Pb) element in the lead halide perovskite solar cells may impede the promotion for such cells, and thus stimulate the search for lead-free perovskite solar cells [5]. All-inorganic and lead-free cesium tin halides ( $\text{CsSnX}_3$ , X = Cl, Br, I) are highly desirable for substituting the organolead halide perovskite solar cells. However, the poor stability of  $\text{CsSnX}_3$  perovskites due to its intrinsic unstable  $\text{Sn}^{2+}$  ions has so far prevented the fabrication of devices that can

withstand sustained operation under normal conditions [6–8]. Recently, a more air-stable compound cesium tin halide perovskite variant, e.g.  $\text{Cs}_2\text{SnI}_6$ , has been reported and employed as hole transport layer (HTL) in dye-sensitized solar cells [9, 10]. Although its exactly physical property is still under investigation [10], it has also been expected to be a promising lead-free perovskite light absorber but without experimental demonstration with solar cell devices till now.

Mesoporous metal oxide films have been usually adopted for solid-state PSCs [12, 13]. But, the difficulty in pore filling has been a persistent issue in such nanoparticle film. One-dimensional (1D) nanorod structure may be better for pore filling with the light absorbing layer than the nanoparticle structure due to its open mesoscopic porous structure [14]. Moreover, nanorod films were reported to possess superior behavior in electron transport for reducing photocarrier recombination, and can help to extend electron diffusion length of the perovskite materials [15–20].

High crystalline ZnO nanorod has been intensively investigated because of its many advantages, such as easily controllable diameter and length and higher electron mobility compared with TiO<sub>2</sub> nanorod [21–24]. Commonly, for perovskite solar cells, the underlying ZnO seed layer acting as both electron collecting layer (ETL) and hole blocking layer is deposited via spin-coating method, which requires a post high-temperature sintering process at ~400 °C and limits its compatibility with flexible plastic substrates. For ZnO nanorod array growth, the seed layer has predominantly influence on its morphology and the interface between ZnO nanorods and fluorine-doped tin oxide (FTO) conductive substrate, which ulteriorly affects the solar cell open-circuit voltage [25]. Therefore, the photovoltaic performance of ZnO nanorod-based PSCs depends significantly on the crystallinity, morphology, and coverage of the ZnO seed layer on FTO substrate.

Pulsed laser deposition (PLD) is generally more powerful in growing high-crystalline dense films with excellent electrical conductivity and repeatability [26, 27]. In this Letter, compact ZnO seed layers are mainly deposited via PLD approach but spin-coating method is also employed in contrast for control experiments. Solid state mesoporous perovskite solar cells based on ZnO nanorod electron transport layers with solution-processed Cs<sub>2</sub>SnI<sub>6</sub> perovskite films as the light absorbing layers are demonstrated. The morphology influence of different nanostructured ZnO nanorod arrays on the photovoltaic performance of Cs<sub>2</sub>SnI<sub>6</sub> based solar cells is also investigated, and an initial PCE of about 1.0% is obtained. This is the first report on the successful use of lead-free Cs<sub>2</sub>SnI<sub>6</sub> in a nanostructured perovskite solar cell.

## 2 Experimental

**2.1 Synthesis of Cs<sub>2</sub>SnI<sub>6</sub>** A mixture of aqueous HI (6.8 mL, 7.58 M) and aqueous H<sub>3</sub>PO<sub>2</sub> (1.7 mL, 9.14 M) and SnI<sub>2</sub> (0.372 g, 1 mM) was completely dissolved at 120 °C using an oil bath. To the hot yellow solution was added CsI (0.260 g, 1 mM). Several minutes later, yellow needle-shaped crystals started to precipitate. By adding 10 mL of acetone, it produces a dark red solution. After 5 min, the stirring was discontinued, and the solution was left to cool to room temperature. The resultant solution washed with degassed EtOH, and then was evaporated to give a dark precipitate.

**2.2 Preparation of perovskite solar cells** Cs<sub>2</sub>SnI<sub>6</sub> powder was completely dissolved in N, N-dimethylformamide (DMF) by stirring the solution. The devices were prepared on cleaned FTO substrates. FTO glass (20 Ω/□) was first etched off a strip of conductive area on the edge side by HCl and Zn powders. The etched substrates were then sequentially cleaned in soap water, acetone, deionized water, and ethanol in ultrasonic bath, and then dried under argon flow. Then the ZnO seed layers were deposited on the cleaned FTO via spin-coating or PLD, respectively, followed by putting the resultant films

in equimolar Zn(NO<sub>3</sub>)<sub>2</sub> and HMTA precursor solution to grow ZnO nanorods. The Cs<sub>2</sub>SnI<sub>6</sub> solution was infiltrated into voids of the nanorods by spin-coating process. The HTM prepared by dissolving 10 mg P3HT into 1 mg chlorobenzene was then deposited by spin-coating at 2500 rpm for 20 s. Finally, 100 nm Ag was thermally evaporated under vacuum as cathode.

**2.3 Characterizations** X-ray diffraction (XRD) patterns were obtained by a Bruker diffractometer (D8-Advance) using Cu K<sub>α</sub> radiation ( $\lambda = 1.5418 \text{ \AA}$ ). The morphologies of the ZnO samples were measured with a scanning electron microscope (SEM, Quanta FEG 250, FEI). The transmittance spectra were recorded using UV–Vis–NIR spectrophotometer (UV-3600, Shimadzu). The solar cell current density versus voltage (*J–V*) characteristics were measured using a Keithley SourceMeter 2612A under AM 1.5G simulated solar illumination with an intensity of 100 mW cm<sup>-2</sup> (3A, San-Ei, calibrated by a NREL-traceable KG5 filtered silicon reference cell). The metal electrodes were measured by a mask and the device area was determined by the overlap of the metal electrodes. Accurate device areas (0.1 cm<sup>2</sup>) were measured device-by-device using a calibrated optical microscope.

**3 Results and discussion** The perovskite Cs<sub>2</sub>SnI<sub>6</sub> material was synthesized by a modified solution route as described by Lee et al. [9]. Briefly, equimolar CsI and SnI<sub>2</sub> were sequentially added into the mixture of aqueous HI and H<sub>3</sub>PO<sub>2</sub> upon heating to 120 °C. Yellow needle-shaped crystals start to precipitate inside the precursor, then black colored Cs<sub>2</sub>SnI<sub>6</sub> powders are obtained after drying, as shown in Fig. 1(a, b). For film growth by spin-coating, the as-prepared Cs<sub>2</sub>SnI<sub>6</sub> powders are then completely dissolved in DMF by continuously stirring the solution. As depicted in inset of Fig. 1(c), the solution is reddish brown and no suspended particles are observed. This solution is injected into the ZnO nanorod arrays and penetrates inside the pores of the ZnO nanorod film. Upon heating, the solvents slowly evaporate and perovskite Cs<sub>2</sub>SnI<sub>6</sub> crystallizes again. The use of this material as light absorber in PSCs is presented later. XRD measurements are shown in Fig. 1(c) for Cs<sub>2</sub>SnI<sub>6</sub> powder sample and solution-processed Cs<sub>2</sub>SnI<sub>6</sub> film on glass substrate. The diffraction peaks at 13.12°, 26.51°, 30.70°, 44.00°, 52.12°, 54.63°, 70.54°, and 72.66° correspond to (111), (222), (400), (440), (622), (444), (662), and (840) lattice planes of the Cs<sub>2</sub>SnI<sub>6</sub> perovskite, respectively, which match well with the reported data [9, 10]. It is worth noting that the solution method yields Cs<sub>2</sub>SnI<sub>6</sub> films containing few weak impurity peaks as depicted in Fig. 1(c). It may derive from the solvents added during the solution growth process, which needs further study. Although such Cs<sub>2</sub>SnI<sub>6</sub> contains minor impurities, the solution process is better for depositing it into the voids among ZnO nanorods in comparison with vapor deposition. The as-prepared Cs<sub>2</sub>SnI<sub>6</sub> film exhibits remarkably sharp absorption onset at a photon energy of 1.45 eV to 1.55 eV.

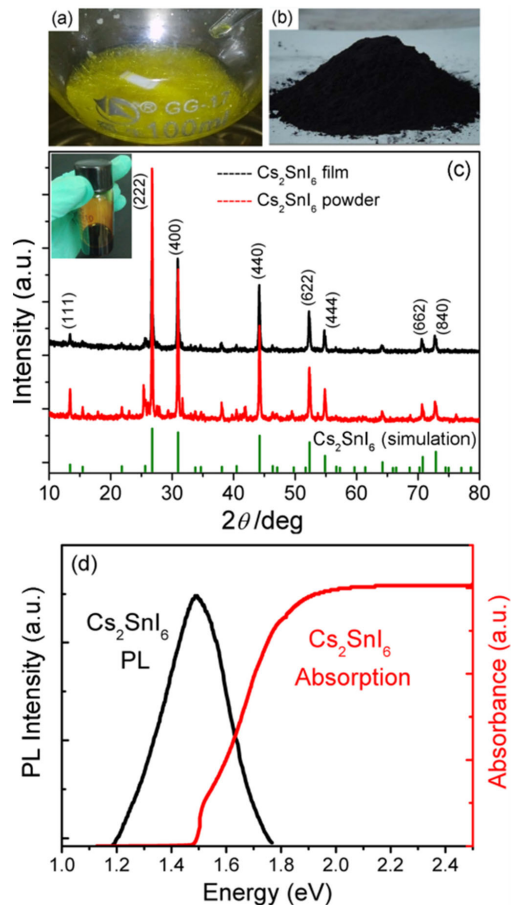


**Figure 1** Digital photographs of (a) the yellow needle-shaped crystals in the precursor liquid and (b) the final black  $\text{Cs}_2\text{SnI}_6$  powders; (c) XRD experimental and simulated patterns of the  $\text{Cs}_2\text{SnI}_6$  powder and film by spin-coating method. Inset shows the solution obtained upon dissolving the powder in DMF. (d) Absorption and photoluminescence (PL) spectra of the  $\text{Cs}_2\text{SnI}_6$  film, indicating its direct bandgap of about 1.48 eV.

By combining its absorption and PL spectra together, a direct optical bandgap of  $\sim 1.48$  eV can be estimated for  $\text{Cs}_2\text{SnI}_6$  (Fig. 1d). This value is slightly bigger than the formerly reported data by only measuring the optical diffuse reflectance spectrum of the  $\text{Cs}_2\text{SnI}_6$  ingots ( $\sim 1.26$  eV) [9]. However, it is smaller than the reported bandgap of  $\text{Cs}_2\text{SnI}_6$  film ( $\sim 1.62$  eV) recently grown by evaporating and annealing CsI in  $\text{SnI}_4$  vapor [11].

Figure 2 shows plan-view and cross-sectional SEM images of the vertically grown ZnO nanorod films, which were synthesized through a typical hydrothermal process [21]. The compact ZnO seed layers were deposited through PLD or spin-coating method, as depicted in Fig. 2(a–d). The nanorods with hexagonal cross section grow nearly perpendicular to the seed layers as shown in Fig. 2(e–h). At the given growth temperature of  $90^\circ\text{C}$  for 120 min, the ZnO nanorod dimensions are mainly influenced by the precursor concentration. The average nanorod diameter increases from about 40 nm to 60 nm, and 80 nm, and the

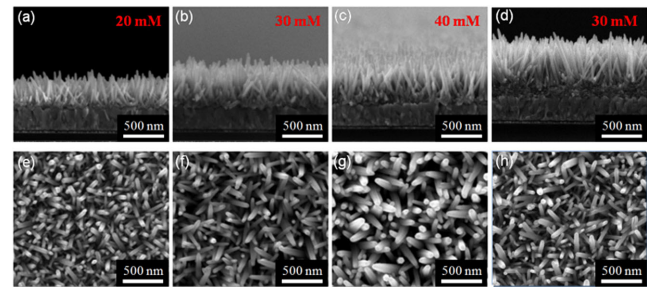


**Figure 2** (a–d) Surface and corresponding (e–h) cross-sectional SEM images of ZnO nanorod arrays grown with precursor solution containing equimolar  $\text{Zn}(\text{NO}_3)_2$  and HMTA of 20 mM, 30 mM, and 40 mM. The ZnO compact seed layers in (a–c) on FTO substrates were deposited with PLD method, and the seed layer in (d) was grown via spin-coating method.

average length varies from  $0.3\ \mu\text{m}$  to  $0.45\ \mu\text{m}$ , and  $0.6\ \mu\text{m}$ , as the precursor concentration increases from 20 mM, 30 mM, to 40 mM, respectively. It is worth to note that the ZnO nanorods have approximately similar length and diameter at the fixed precursor concentration of 30 mM although different ZnO seed layers were used Fig. 2(b) and (d). The XRD patterns in Fig. S1 of the Supporting Information (SI) show the highly oriented nature of ZnO nanorods. The strongest (002) peak reflects that *c*-axis elongated nanorods are oriented normal to the FTO substrate. ZnO nanorods exhibit strong near bandgap absorption at 370 nm (Figs. S2, SI), which indicates the ZnO nanorod has a band gap of  $\sim 3.3$  eV [28]. The nanorod grown on the PLD-based seed layer shows enhanced transmittance compared with that of spin-coating method, which is attributed to its more ordered vertical alignment and the reduced Rayleigh light scattering [29].

Figure 3(a) depicts the device structure of the lead-free  $\text{Cs}_2\text{SnI}_6$ -based nanorod solar cell, in which compact PLD grown ZnO layer is used as ETL and ZnO nanorods array is adopted as scaffold for the deposition of  $\text{Cs}_2\text{SnI}_6$  film, and the poly(3-hexylthiophene-2,5-diyl) (P3HT) capping film acts as HTL. Energy level diagram of each layer is also presented in Fig. 3(a), and the alignments of conduction and valence bands of the  $\text{Cs}_2\text{SnI}_6$  [9] permit electrons injecting into the ZnO nanorods and holes transporting to the P3HT layer, as well as the according front/back contacts.

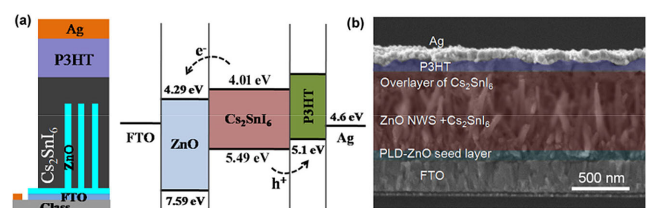


**Figure 3** Device and energy band structures of the FTO/seed layer/ZnO nanorods/ $\text{Cs}_2\text{SnI}_6$ /P3HT/Ag solar cell. (a) Diagram of the device configuration and energy band levels. (b) Cross-sectional SEM image of the complete device structure. The various layers are marked with different colors.

The complete all solid-state PSC structure viewed via cross-sectional SEM image Fig. 3(b) indicates the infiltration of Cs<sub>2</sub>SnI<sub>6</sub> into the voids among the nanorods and the top Ag electrode is well separated from the photoanode by the P3HT layer. The PLD-ZnO seed layer tinted with light green is also expected to play a role in preventing the direct contact between FTO and P3HT. The spin-coating technology leads to the formation of an overlayer (capping layer) of Cs<sub>2</sub>SnI<sub>6</sub> perovskite on top of the ZnO nanorod film, as can be seen in Fig. 3(b). The resulted devices corresponding to Fig. 2(a–d) were also shown in Fig. S3(a–d). Voids are partly found in the ZnO nanorod arrays, indicating incomplete pore filling with the perovskite (Figs. S3, SI). Obviously, pores are relatively well filled by the perovskite Cs<sub>2</sub>SnI<sub>6</sub> for the shorter nanorod films as shown in Fig. S3(a), (b), (d) compared with the longer nanorod film of Fig. S3(c).

Besides the seed layer, the length of ZnO nanorod also influences the device performance, which can be optimized by careful control of the precursor concentration. Taking the seed layers prepared via PLD as an example, the influence of the precursor concentration on the ZnO nanorods and the corresponding photovoltaic performance was investigated, as shown in Fig. 4(b) and Table 1. The solar cell PCE is firstly enhanced to 0.86% with increasing precursor concentration, but degrades to 0.21% when the precursor concentration was as high as 40 mM. Short-circuit current density ( $J_{sc}$ ) is remarkably altered by the precursor concentration, where  $J_{sc}$  is highest for 30 mM-ZnO nanorods ( $J_{sc} = 3.20 \text{ mA/cm}^2$ ), while the 20 mM exhibits inter-

**Table 1** Photovoltaic parameters of short-circuit photocurrent density ( $J_{sc}$ ), open-circuit voltage ( $V_{oc}$ ), fill factor (FF), and power conversion efficiency ( $\eta$ ), depending on precursor concentration and different methods used for growing ZnO compact layer.

sample/parameters	$J_{sc}$ (mA/cm <sup>2</sup> )	$V_{oc}$ (V)	FF	$\eta$ (%)
20 mM-PLD	2.56	0.47	43.25	0.54
30 mM-PLD	3.20	0.52	51.50	0.86
40 mM-PLD	1.11	0.48	37.97	0.21
30 mM-spin-coating	3.08	0.42	43.06	0.56

mediate value ( $J_{sc} = 2.56 \text{ mA/cm}^2$ ) and 40 mM shows the lowest  $J_{sc}$  of  $1.11 \text{ mA/cm}^2$ . It is noted that open-circuit voltage ( $V_{oc}$ ) changing between 0.47 V and 0.52 V is observed, indicating  $V_{oc}$  is hardly altered by the precursor concentration. The decrease in  $J_{sc}$  is most likely to be related to the amount of the deposited Cs<sub>2</sub>SnI<sub>6</sub> perovskite. Upon improved length and pore size of the ZnO nanorod arrays with appropriately increasing the precursor concentration, pore filling fraction (PFF) is enhanced. This leads to larger amount of perovskite absorber penetrated into the voids, and consequently, significantly increases the  $J_{sc}$  [18]. In contrast, incomplete pore filling was observed (Figs. S3c, SI) when 40 mM precursor concentration was used for ZnO nanorod growth with a result of sharp decrease in  $J_{sc}$ .

It is well known, with PLD method, the morphology and physical property of the deposited layers can be appropriately controlled by adjusting the deposition parameters, such as the oxygen partial pressure [30, 31]. At a pressure of 2.0 Pa, an ordered, column-shaped ZnO seed layer was formed (Fig. 4a). However, with spin-coating method, the surface of the ZnO seed layer is relatively rough with many voids, showing similar morphology to that of the typical mesoscopic film structure. To further address the influence of the ZnO seed layer growth method on the device performance, devices with an identical structure were fabricated based on two films grown with PLD and spin-coating method, respectively. Their corresponding  $J$ - $V$  curves and IPCE spectra were investigated as shown Fig. 4(b) and Fig. S4 (SI). The device with PLD-ZnO seed layer demonstrates better performance (PCE ~ 0.86%) than the device (PCE ~ 0.56%) employing spin-coated seed layer. Substantial improvement was simultaneously observed in  $V_{oc}$  from 0.42 V to 0.52 V and FF from 43.06% to 51.50%. All of these indicate that noticeably alleviative carrier recombination within the Cs<sub>2</sub>SnI<sub>6</sub> perovskite due to the efficient electron extraction and hole blocking process in the PLD-ZnO seed layer with enhanced crystallinity, as illustrated in Fig. 4(a).

Several future works are expected to help obtain higher efficiencies in these solar cells. First, the purity and polycrystalline quality of Cs<sub>2</sub>SnI<sub>6</sub> can be further improved. The precursor concentration, solvent, doping, and deposition temperature can be further optimized. The second direction

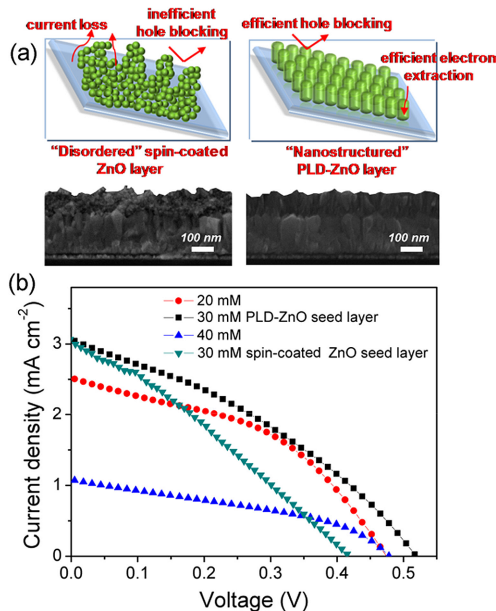


**Figure 4** Influence of the morphology and growth method of ZnO seed layers on the solar cell performance. (a) Schematic illustrations and cross-sectional SEM images of disordered and nanostructured ZnO films grown with different methods. (b) The  $J$ - $V$  curves of the Cs<sub>2</sub>SnI<sub>6</sub> perovskite solar cells with ZnO nanorods grown on different seed layers and with different precursors.

is to substantially reduce the series resistance and to enhance the shunt resistance by optimizing the electron and hole transporting layers growth. More importantly, the in-state dynamics of the photoexcited electrons and holes in  $\text{Cs}_2\text{SnI}_6$  and the fundamental properties of  $\text{Cs}_2\text{SnI}_6$  like carrier diffusion lengths should be studied, which is the most critical question concerning whether mesostructured (in this paper) or planar heterojunction perovskite solar cells will eventually dominate the device structure.

**4 Conclusions** In conclusion, we have synthesized lead-free perovskite  $\text{Cs}_2\text{SnI}_6$  powder through a modified solution process and demonstrated its application as absorbing layer in mesoporous solar cell with a configuration of FTO/ZnO compact layer/nanorods/ $\text{Cs}_2\text{SnI}_6$ /P3HT/Ag. This is the first attempt to fabricate nanostructured  $\text{Cs}_2\text{SnI}_6$ -based perovskite solar cells. The influences of ZnO seed layers and nanorod morphology on the device photovoltaic performance were also investigated. With careful control of ZnO nanorod length and pore size to ensure high loading of the  $\text{Cs}_2\text{SnI}_6$  absorber, we achieved a PCE of near 1%. Moreover, the PLD-ZnO seed layer with optimized surface morphology was demonstrated to be more efficiently suppress charge recombination, and resulted in higher PCE than that of the device utilizing spin-coated ZnO seed layer. These results presented here for  $\text{Cs}_2\text{SnI}_6$  light absorber based solar cell may further help to elucidate potential suitability of this perovskite for lead-free PV technology.

**Supporting Information** Additional supporting information may be found in the online version of this article at the publisher's website.

**Acknowledgements** This work is supported by NSFC (51472110, 11174112) and Shandong Provincial Natural Science Foundation (2014ZRB01A0P, 2014ZRB01A47).

## References

- [1] B. Jeong, S. M. Cho, S. H. Cho, J. H. Lee, I. Hwang, S. K. Hwang, J. H. Cho, T. W. Lee, and C. Park, *Phys. Status Solidi A* **10**, 381 (2016).
- [2] H. S. Kim, C. R. Lee, J. H. Im, K. B. Lee, T. Moehl, A. Marchioro, S. J. Moon, R. Humphry-Baker, J. H. Yum, J. E. Moser, M. Grätzel, and N. G. Park, *Sci. Rep.* **2**, 00591 (2012).
- [3] M. M. Lee, J. Teuscher, T. Miyasaka, T. N. Murakami, and H. J. Snaith, *Science* **643**, 338 (2012).
- [4] S. K. Yang, J. H. Noh, N. J. Jeon, Y. C. Kim, S. Ryu, J. Seo, and S. I. Seok, *Science* **348**, 1234 (2015).
- [5] F. Hao, C. C. Stoumpos, D. H. Cao, R. P. H. Chang, and M. G. Kanatzidis, *Nature Photon.* **8**, 489 (2014).
- [6] M. H. Kumar, S. Dharani, W. L. Leong, P. P. Boix, R. R. Prabhakar, T. Baikie, C. Shi, H. Ding, R. Ramesh, M. Asta, M. Grätzel, S. G. Mhaisalkar, and N. Mathews, *Adv. Mater.* **26**, 7122 (2014).
- [7] Z. W. Xiao, Y. Y. Zhou, H. Hosono, and T. Kamiya, *Phys. Chem. Chem. Phys.* **17**, 18900 (2015).
- [8] C. C. Stoumpos, C. D. Malliakas, and M. G. Kanatzidis, *Inorg. Chem.* **52**, 9019 (2013).
- [9] B. Lee, C. C. Stoumpos, N. Zhou, F. Hao, C. Malliakas, C. Y. Yeh, T. J. Marks, M. G. Kanatzidis, and R. P. Chang, *J. Am. Chem. Soc.* **136**, 15379 (2014).
- [10] N. Chander, P. S. Chandrasekhar, and V. K. Komarala, *RSC Adv.* **4**, 55658 (2014).
- [11] B. Saparov, J. P. Sun, W. W. Meng, Z. W. Xiao, H. S. Duan, O. Gunawan, D. Shin, I. G. Hill, Y. F. Yan, and D. B. Mitzi, *Chem. Mater.* **28**, 2315 (2016).
- [12] M. M. Lee, J. Teuscher, T. Miyasaka, T. N. Murakami, and H. J. Snaith, *Science* **338**, 643 (2012).
- [13] N. Yantara, D. Sabba, F. Yanan, J. M. Kadro, T. Moehl, P. P. Boix, S. Mhaisalkar, M. Gratzeld, and C. Grätzel, *Chem. Commun.* **51**, 4603 (2015).
- [14] H. J. Snaith, H. B. Robert, P. Chen, I. Cesar, S. M. Zakeeruddin, and M. Grätzel, *Nanotechnology* **19**, 424003 (2008).
- [15] X. Feng, K. Shankar, O. K. Varghese, M. Paulose, T. J. Latempa, and C. A. Grimes, *Nano Lett.* **8**, 3781 (2008).
- [16] B. Liu and E. S. Aydil, *J. Am. Chem. Soc.* **131**, 3985 (2009).
- [17] E. Hendry, M. Koeber, B. O'Regan, and M. Bonn, *Nano Lett.* **6**, 755 (2006).
- [18] H. S. Kim, J. W. Lee, N. Yantara, P. P. Boix, S. A. Kul-karni, S. Mhaisalkar, M. Grätzel, and N. G. Park, *Nano Lett.* **13**, 2412 (2013).
- [19] J. Qiu, Y. Qiu, K. Yan, M. Zhong, C. Mu, H. Yan, and S. Yang, *Nanoscale* **5**, 3245 (2013).
- [20] S. Dharani, H. K. Mulmudi, N. Yantara, P. T. T. Thrang, N. G. Park, M. Grätzel, S. Mhaisalkar, N. Mathews, and P. P. Boix, *Nanoscale* **6**, 1675 (2014).
- [21] M. H. Kumar, N. Yantara, S. Dharani, M. Grätzel, S. Mhaisalkar, P. P. Boix, and N. Mathews, *Chem. Commun.* **49**, 11089 (2013).
- [22] D. Bi, G. Boschloo, S. Zmuller, S. L. Yang, E. M. J. Johansson, and A. Hagfeldt, *Nanoscale* **5**, 11686 (2013).
- [23] Q. Zhang, C. S. Dandeneau, X. Zhou, and G. Cao, *Adv. Mater.* **21**, 4087 (2009).
- [24] Q. Zhang, T. R. Chou, B. Russo, S. A. Jenekhe, and G. Cao, *Angew. Chem.* **47**, 2402 (2008).
- [25] D. Y. Son, K. H. Bae, H. S. Kim, and N. G. Park, *J. Phys. Chem. C* **119**, 10321 (2015).
- [26] D. J. Late, P. A. Shaikh, R. Khare, R. V. Kashid, M. Chaudhary, M. A. More, and S. B. Ogale, *ACS Appl. Mater. Interfaces* **6**, 15881 (2014).
- [27] J. H. Park, J. Seo, S. Park, S. S. Shin, Y. C. Kim, N. J. Jeon, H. W. Shin, T. K. Ahn, J. H. Noh, S. C. Yoon, C. S. Hwang, and S. I. Seok, *Adv. Mater.* **27**, 4013 (2015).
- [28] W. I. Park and G. C. Yi, *Adv. Mater.* **16**, 87 (2004).
- [29] H. Park, K.-J. Byeon, K.-Y. Yang, J. Y. Cho, and H. Lee, *Nanotechnology* **21**, 355304 (2010).
- [30] J. H. Noh, J. H. Park, H. S. Han, D. H. Kim, B. S. Han, S. Lee, J. Y. Kim, H. S. Jung, and K. S. Hong, *J. Phys. Chem. C* **116**, 8102 (2012).
- [31] J. H. Park, D. H. Kim, S. S. Shin, H. S. Han, M. H. Lee, H. S. Jung, J. H. Noh, and K. S. Hong, *Adv. Energy Mater.* **4**, 1 (2014).